Assessment of digital image correlation measurement errors: methodology and results

Michel Bornert, Fabrice Brémand, Pascal Doumalin, Jean-Christophe Dupré, Marina Fazzini, Michel Grédia, François Hild, Sebastien Mistou, Jérôme Molimard, Jean-José Orteu, et al.

To cite this version:

Michel Bornert, Fabrice Brémand, Pascal Doumalin, Jean-Christophe Dupré, Marina Fazzini, et al.. Assessment of digital image correlation measurement errors: methodology and results. Experimental Mechanics, Society for Experimental Mechanics, 2009, 49, pp.353-370. <10.1007/s11340-008-9204-7>. <hal-00881043>

HAL Id: hal-00881043

https://hal.archives-ouvertes.fr/hal-00881043

Submitted on 7 Nov 2013

To link to this article: DOI:10.1007/s11340-008-9204-7
http://dx.doi.org/10.1007/s11340-008-9204-7

To cite this version:

Bornert, Michel and Brémand, Fabrice and Doumalin, Pascal and Dupré, Jean-Christophe and Fazzini, Marina and Grédiac, Michel and Hild, François and Mistou, Sebastien and Molimard, Jérôme and Orteu, Jean-José and Robert, Laurent and Surrel, Yves and Vacher, Pierre and Wattrisse, Bertrand *Assessment of digital image correlation measurement errors: methodology and results.* (2009) Experimental Mechanics, vol. 49 (n° 3). pp. 353-370. ISSN 0014-4851

Assessment of Digital Image Correlation measurement errors: methodology and results

M. Bornert F. Brémand P. Doumalin J.-C. Dupré M. Fazzini
M. Grédiac F. Hild S. Mistou J. Molimard J.-J. Orteu * L. Robert
Y. Surrel P. Vacher B. Wattrisse

Workgroup “Metrology” of the French CNRS research network 2519
“Mesures de Champs et Identification en Mécanique des Solides /
Full-field measurements and identification in solid mechanics”

http://www.ifma.fr/lami/gdr2519

November 14, 2008

---

*Corresponding author. Fax: +33 563 493 099. *E-mail:* Jean-Jose.Orteu@enstimac.fr

M. Bornert
Laboratoire de Mécanique des Solides, CNRS - UMR7649, Department of Mechanics, Ecole polytechnique, 91128 Palaiseau, France

F. Brémand - P. Doumalin- J.-C. Dupré
LMS, UMR 6610, Université de Poitiers, 86962 Futuroscope Chasseneuil, France

M. Fazzini - S. Mistou
ENIT, Tarbes, France

M. Grédiac
LaMI, Université Blaise Pascal-IFMA, Clermont-Ferrand, France

F. Hild
LMT, ENS Cachan, Cachan, France

J. Molimard
SMS, Ecole Mines St Étienne, St Étienne, France

J.-J. Orteu - L. Robert
Université de Toulouse, Ecole Mines Albi, CROMeP, 81013 Albi, France

Y. Surrel
Visuol Technologies, Metz, France

P. Vacher
SYMME, Université de Savoie, Annecy, France

B. Wattrisse
LMGC, Université Montpellier II, Montpellier, France

Abstract: Optical full-field measurement methods such as Digital Image Correlation (DIC) are increasingly used in the field of experimental mechanics, but they still suffer from a lack of information about their metrological performances. To assess the performance of DIC techniques and give some practical rules for users, a collaborative work has been carried out by the Workgroup "Metrology" of the French CNRS research network 2519 "MCIMS"[1]. A methodology is proposed to assess the metrological performances of the image processing algorithms that constitute their main component, the knowledge of which being required for a global assessment of the whole measurement system. The study is based on displacement error assessment from synthetic speckle images. Series of synthetic reference and deformed images with random patterns have been generated, assuming a sinusoidal displacement field with various frequencies and amplitudes. Displacements are evaluated by several DIC packages based on various formulations and used in the French community. Evaluated displacements are compared with the exact imposed values and errors are statistically analyzed. Results show general trends rather independent of the implementations but strongly correlated with the assumptions of the underlying algorithms. Various error regimes are identified, for which the dependence of the uncertainty with the parameters of the algorithms, such as subset size, gray level interpolation or shape functions, is discussed.

Keywords: Digital image correlation – Error assessment – Spatial resolution – Displacement resolution – Uncertainty assessment – Benchmark – Speckle pattern – Texture

---

[1] MCIMS: Mesures de Champs et Identification en Mécanique des Solides / Full-field measurement and identification in solid mechanics, `http://www.ifma.fr/lami/gdr2519`

1 Introduction

Optical full-field measurement techniques are very promising tools for the experimental analysis of the mechanical properties of materials and structures. The main techniques are photoelasticity, moiré, holographic and speckle interferometry, grid method and digital image correlation (DIC) [1–6].

Even though they are more and more used, they still suffer from the lack of a complete metrological characterization. Some papers have been recently published on this subject. They deal with the evaluation of optical systems for full-field strain measurement based on standard experimental test on standard specimens [7,8]. Such techniques rely on complex measurement chains, so the error sources of each of its elements require proper evaluations before a global assessment of the measurement. Thus a clear-cut separation should be made between kinematic fields measured by these techniques and the mechanical modeling and testing.

Digital image correlation (DIC) has shown over twenty years to be a very valuable tool for full-field displacement measurements [9–28]. It consists in recording with a camera some digital images of a specimen undergoing a mechanical transformation and applying an image correlation algorithm with an appropriate software. An important, but not unique, element of the measurement procedure is the image analysis software package which is supposed to provide an apparent 2-D displacement field that maps a so-called "reference image" to a "deformed image" at a discrete set of positions, according to some principle of optical flow conservation.

This technique is among the most popular optical methods, because of the availability of commercial packages, the constantly shrinking cost of digital cameras and computers, and the general (apparent) simplicity of sample preparation and optical setup. The surface preparation is usually very simple, namely, either no preparation is needed (if the material texture of the surface has enough contrast), or a random speckle pattern has to be applied, which is handily performed by spray painting the specimen.

However, the user is often confused by the number of parameters that have to be set in a DIC measurement, namely, speckle size and "density" correlation criteria and algorithm of optimization, subset (or correlation window) size, pitch or subset overlap, gray level interpolation, etc. It is usually not clear for the user how the choices he/she makes influences the quality of the results obtained. This is the reason why a number of research groups have joined forces to investigate in a systematic way how the different DIC parameters influence the measured displacement fields. This common action takes place in the "Metrology" workgroup of GDR 2519 MCIMS [29] created in January 2003 by the CNRS, the French national center for scientific research.

The main point of the paper is to discuss a general procedure to assess the measurement errors of the DIC method and to apply this procedure, by using several DIC codes, in order to get general trends enabling a person to choose the DIC parameters for a given application.

The proposed methodology is based on synthetic images undergoing sinusoidal displacements with various amplitudes and spatial frequencies. Displacements are evaluated by six DIC packages for various DIC parameters. The measured displacements are compared to prescribed ones. Results are analyzed and commented. The outline of the paper is the following. In Section 2, the proposed methodology for the DIC error assessment is described. In Section 3, the results are presented. Section 4 discusses five aspects related to ultimate error, subset size, speckle size, gray level interpolation and shape functions.

2 DIC Error Assessment

Quantitative evaluations of the errors of DIC measurements are usually limited to situations dealing with homogeneous mechanical transformations, namely, rigid body translations, planar rotations, or out-of-plane rigid body motions. They result in apparent essentially affine transformations of the 2-D image [14, 17, 19, 26, 30, 31]. Some authors use synthetic images that mimic real patterns to compute displacements in the Fourier [30] or space [17,19,32,33] domains. Results present generally the well-known "sinusoidal" dependence of the displacement error with the sub-pixel value of the prescribed displacement [14]. Some other authors record a speckle image of an actual experiment and apply artificially imposed displacements [26,31]. For instance, in Ref. [31] it is observed that the mean of the standard displacement uncertainties decreases as the subset size increases with a power law variation, showing that the displacement uncertainty and the spatial resolution are always the result of a compromise.

Very few studies [19,34–37] address situations with spatially fluctuating displacement fields. Such fields are needed to investigate a quantitative assessment of the spatial resolution of DIC techniques. Since it is very difficult, and in practice almost impossible, to experimentally generate non-uniform deformation fields with precisely prescribed strains —some authors have recently investigated this way e.g. [7, 8]— , it is generally necessary to perform the analysis with simulated images obtained with some algorithms that mimic as closely as possible the generation of images with a real camera. Quadratic displacement fields are considered on synthetic images in Ref. [34]. The authors show that no systematic displacement error is observed if a second order shape function is used. They claim that the correlation function is minimized when the difference between the shape function and the actual displacement field encoded in the images is minimized.

The present approach aims at extending the analysis by using synthetic speckle images that display well-controlled planar sinusoidal displacements with different spatial frequencies. The reason for this particular choice is that the displacement field and all its spatial derivatives vary with the spatial coordinates. As a consequence, the transformation cannot be described exactly by standard polynomial shape functions, so that the proposed analysis more closely reflects real situations. For simplicity, it was chosen to apply a displacement only along one direction. This choice allows one to study the local performances in terms of statistical properties. In the following, only performances in terms of displacements are reported. On the one hand, this is the actually measured quantity as opposed to strains that are post-processed in various ways depending on any particular correlation code. On the other hand, a sinusoidal displacement has already complex spatial variations that are representative of what a user would like to measure, namely local kinematic fluctuations. In the sequel, the chosen methodology is detailed. First, the main features of the prescribed displacement is presented. Second, the generation of artificial pictures is discussed. Third, the procedure for analyzing the correlation results is introduced. Last, the correlation parameters that were tested are defined.

2.1 Prescribed displacement field

The main idea is to use the usual tools for systems analysis for this “black box” characterization. By spatial Fourier transform, an arbitrary displacement field is decomposed over a set of single spatial frequency components, each of them exhibiting a given direction, amplitude, frequency and phase. The usual method to describe linear systems is to give their frequency response function, that indicates how each single frequency component of the input signal is changed in terms of amplitude and phase by going through the system.

Even if DIC is not a linear system, this procedure allows to give a good description of the behavior of the DIC system. Furthermore, it estimates the link between measurement errors and spatial frequencies of the input signal. This is necessary for a quantitative assessment of the spatial resolution of DIC.

The proposed methodology is similar to that leading to the Modulation Transfer Function (MTF) classically used to characterize optical devices, namely, the errors of the displacements obtained with various DIC algorithms are evaluated as functions of the spatial frequencies and the amplitude of a sinusoidal displacement field.

Deformed images are obtained assuming only a unidirectional in-plane sinusoidal displacement (elongation/contraction displacements along the X-direction with a zero Y-displacement). The displacement is given by

$$\underline{u}(\underline{X}) = \alpha p \sin\left(\frac{2\pi X}{p}\right) \underline{e}_X \tag{1}$$

where p is the period in pixels and $2\pi\alpha$ the amplitude of the variation of the XX component of the displacement gradient. The components of the first and second displacement gradients along the X-direction are expressed as follows

$$u_{,X}(\underline{X}) = \frac{\partial u}{\partial X} = 2\pi\alpha \cos\left(\frac{2\pi X}{p}\right) = u_{,X}^{Max} \cos\left(\frac{2\pi X}{p}\right) \tag{2}$$

$$u_{,XX}(\underline{X}) = \frac{\partial^2 u}{\partial X^2} = \frac{-4\pi^2\alpha}{p} \sin\left(\frac{2\pi X}{p}\right) = -u_{,XX}^{Max} \sin\left(\frac{2\pi X}{p}\right) \tag{3}$$

with $u_{,X}^{Max} = 2\pi\alpha$ and $u_{,XX}^{Max} = 4\pi^2\alpha/p$. Values chosen for the amplitude α and for the period p are respectively $\alpha \in \{0.02, 0.01, 0.005, 0.001\}$ and $p \in \{10, 20, 30, 60, 130, 260, 510\}$ pixels, for 512×512 pixel images. Note that corresponding values of the maximum displacement gradient are 12.6%, 6.3%, 3.1%, 0.63%, respectively.

2.2 Image generation

It is chosen to separate the displacements calculation from all other experimental features to investigate the 2-D correlation algorithms by themselves, and thus synthetic 512×512 pixel images are used as input to know exactly the information encoded. The idea is to input a set of well chosen images and to evaluate the deviations between the correlation software output and the displacement field that was used during image generation.

2.2.1 Speckle-pattern images generation

The set of synthetic speckle-pattern images is obtained using the TexGen software [38]. This software has been developed to produce synthetic speckle-pattern images which mimic as realistically as possible real DIC speckle patterns, obtained for instance with spray painting, or toner powder deposits. Deformed speckle-pattern images are also generated with a deformation field of arbitrary type. The software has been designed to limit the introduction of any bias due to interpolation.

Details of the speckle-pattern generator algorithm are not provided herein (see Ref. [38]). Perlin's coherent noise function [39] is used to generate a continuous noise function $t = noise(x, y),\ x \in \mathcal{R},\ y \in \mathcal{R}$. Some transformations are applied to this basic noise function in order to generate a texture function that mimic one desired speckle pattern appearance with control of the speckle size. The speckle-pattern image is generated by a photometric mapping and an 8-bit digitization of the texture function computed for each integer pixel of the image. The integration of the texture function over the domain corresponding to the sensitive photometric material of one pixel is performed by a super-sampling technique (for anti-aliasing). A reference speckle-pattern image represented by a gray level function $I_r(\underline{X})$ is first generated. A deformed speckle-pattern image is then generated. It is represented by a gray level function $I_d(\underline{x})$ by applying any given material transformation Φ_M using the optical flow conservation

$$I_d(\underline{x}) = I_r(\Phi_M^{-1}(\underline{x})), \tag{4}$$

with $\Phi_M(\underline{X}) = \underline{X} + \underline{u}(\underline{X})$. It should be noted that transformation Φ_M is applied to the continuous texture function, and not to the discrete pixel gray level values of the reference image. This leads to a continuous deformed texture that is mapped to the deformed image. Regarding procedures emanating from classical approaches, based for instance on Fourier transform [30] or any other interpolation scheme, this procedure limits the introduction of any bias due to interpolation. The "texture to image" mapping function is the same for the reference and deformed images. Fig. 1 shows some examples of sub-images (512 × 100 pixel images) of both the reference and deformed images. They are obtained for $p = 130$ pixels and $\alpha = 0.1$, 0.05 and 0.02, respectively.

[Figure 1 about here.]

2.2.2 Speckle characterization

First, gray level histogram is adjusted to obtain a broad distribution covering all the 256 gray levels. Then, attention is paid to the speckle size, i.e. the grain size of the speckle pattern. One way to estimate the mean size of a speckle pattern is to perform image morphology analysis [36]. Another way is to compute the autocorrelation radius, based on the autocorrelation function of the speckle image [40,41]. In this work, the autocorrelation radius r is the radius at half height of the normalized autocorrelation function of the reference image (see Fig. 2).

The speckle pattern mean size has been adjusted in order to study the influence of the speckle pattern size on the DIC measurement accuracy. Fine ($r = r_s/2$), medium ($r = r_s$) or coarse ($r = 2r_s$) patterns are produced, as presented in Fig. 2. The medium pattern is characterized by the standard size $r_s = 2.2$ pixels.

[Figure 2 about here.]

2.3 Procedure for analyzing the results

Displacements are evaluated with various DIC formulations on a regular $N \times N$ square grid defined in the initial 512×512 pixels image, with pitches $(dx, dy = d)$ such that subsets at adjacent positions do not overlap, thus ensuring the statistical independence of the corresponding errors. In practice dx is even and equal to d or $d + 1$, where d is the subset size.

Square subsets of different sizes d are used, namely, 9 or 10, 15 or 16, 21 or 22 and 31 or 32 pixels (some softwares accept only even or odd pixel subset sizes). Computed displacements are compared to prescribed ones at all grid positions and discrepancies are analyzed statistically in terms of root mean square, standard deviation and bias. This analysis is performed globally for all points in the image but also locally, columns by columns for each set of points exhibiting the same X coordinate, displacement and displacement gradients. It could be shown that the results are calculated from a sufficiently large number of points to ensure their statistical reliability, both in the global and local analyzes, even for the largest subset sizes associated with the smallest data sets.

Displacement errors at the center of a subset of coordinates (i, j) are defined by

$$\Delta u(i,j) = u_{imposed}(i,j) - u_{measured}(i,j)$$
$$\text{with} \quad \begin{cases} i = \frac{dx}{2}, ..., (N-1)d_x + \frac{dx}{2} \\ j = \frac{dy}{2}, ..., (N-1)d_y + \frac{dy}{2} \end{cases} \tag{5}$$

For the global approach, the square root of the mean square error (RMS error) is defined by

$$RMS_G = \sqrt{\frac{1}{n}\sum_{i,j}\left[\Delta u(i,j)\right]^2} = \sqrt{\frac{n-1}{n}\sigma_G{}^2 + \overline{\Delta u_G}^2} \tag{6}$$

where n is the number of calculated values ($n \leq N^2$, because of possible non computed values), σ_G

and $\overline{\Delta u}_G$ the global standard deviation and arithmetic mean, respectively

$$\sigma_G = \sqrt{\frac{n\sum_{i,j}\left[\Delta u(i,j)\right]^2 - \left[\sum_{i,j}\Delta u(i,j)\right]^2}{n(n-1)}} \quad \text{and} \quad \overline{\Delta u}_G = \frac{1}{n}\sum_{i,j}\Delta u(i,j). \tag{7}$$

For the local investigation, the standard deviation along a given column i is expressed as

$$\sigma_L(i) = \sqrt{\frac{n_i\sum_{j}\left[\Delta u(i,j)\right]^2 - \left[\sum_{j}\Delta u(i,j)\right]^2}{n_i(n_i-1)}} \tag{8}$$

where n_i is the number of calculated values in the i^{th} column, and the local arithmetic mean is given by

$$\overline{\Delta u}_L(i) = \frac{1}{n_i}\sum_{j}\Delta u(i,j). \tag{9}$$

The local root mean square thus reads

$$RMS_L(i) = \sqrt{\frac{1}{n_i}\sum_{j}\left[\Delta u(i,j)\right]^2} = \sqrt{\frac{n_i-1}{n_i}\sigma_L(i)^2 + \overline{\Delta u}_L(i)^2}. \tag{10}$$

Since the imposed displacements and gradients are constant along the columns of each image, it is possible to analyze the above quantities versus the displacement and displacement gradients.

These results are given and discussed in section 3, as a function of various DIC parameters summarized in the following section.

2.4 DIC formulations and parameters

The general purpose of DIC algorithms is to determine the mechanical transformation Φ_M from the knowledge of the gray level distributions I_r and I_d in the reference and deformed configurations, discretized into image pixels with a given bit depth, assuming that relation (4) is satisfied. As such, this so-called "optical flow determination" problem, is an ill-posed inverse problem [42] which is only solved approximately with additional assumptions. In classical DIC algorithms, the reference image is decomposed into usually square small domains $\mathcal{D}$ (the correlation window or subset) on which Φ_M is approximated by a local map Φ, also called shape function, which belongs to a family $\mathcal{E}_\mathcal{D}$ of continuous displacement functions, described by a limited number of scalar parameters. The general algorithm consists in determining these parameters by minimizing a correlation coefficient $C(\Phi)$, for which various definitions can be adopted [45] and which measures the disparity between the gray level distribution in the domain $\mathcal{D}$ in the reference image and the distribution in the deformed image back-convected to reference image according to Φ, as

$$\Phi \approx \underset{\Phi \in \mathcal{E}_{\mathcal{D}}}{\text{Arg}\min} C(\Phi). \tag{11}$$

In addition to the size d of the subset characterizing the optical signature of a material domain and the resolution of the image (associated with the speckle size r), the various DIC algorithms for the evaluation of displacement field depend on specific choices of correlation coefficient, shape function, optimization algorithm and interpolation function required to evaluate sub-pixel displacement from images described with a pixel resolution. These parameters are briefly recalled in the following with an emphasis on those whose influence has been investigated with the proposed methodology. Other parameters, in particular the definition of the correlation coefficient, were observed to have a very limited influence on the results as the simulated images satisfy the optical flow conservation (Eq. (4)) and are noiseless.

2.4.1 Subset shape function Φ

The material transformation of the subset is usually approximated by a polynomial expression. Even though higher order formulations can be found in the literature [43], the most general expression used in this study is a second order polynomial [44], given by:

$$\left\{ \begin{array}{rl} u(X,Y) = & a_1 + a_3\Delta X + a_5\Delta Y + a_7\Delta X\,\Delta Y + a_9\Delta X^2 + a_{11}\Delta Y^2 + a_{13}\Delta X^2\Delta Y \cdots \\ & \cdots + a_{15}\Delta X\Delta Y^2 + a_{17}\Delta X^2\Delta Y^2 \\ v(X,Y) = & a_2 + a_4\Delta X + a_6\Delta Y + a_8\Delta X\,\Delta Y + a_{10}X^2 + a_{12}\Delta Y^2 + a_{14}\Delta X^2\Delta Y \cdots \\ & \cdots + a_{16}\Delta X\Delta Y^2 + a_{18}\Delta X^2\Delta Y^2 \end{array} \right. \tag{12}$$

where $\Delta X = X - X_0$, $\Delta Y = Y - Y_0$, (X_0, Y_0) being the center of subset $\mathcal{D}$. The simplest shape function corresponds to a zero order polynomial [10] associated with pure translation ($a_i = 0,\ \forall i > 2$). First order or strictly affine shape function [11] are obtained with $a_i = 0,\ \forall i > 6$, while bilinear transformation uses the first 8 coefficients [16]. Finally, full bi-quadratic approximation makes use of all 18 coefficients while quadratic are restricted to the first 12 coefficients. For the sake of simplicity, both strictly affine and bilinear transformations on the one hand, and quadratic and bi-quadratic transformations on the other hand, will not be distinguished here since their results were similar in the context of the present study where only uniaxial transformations are considered. Note that recent extensions of DIC procedures make use of globally continuous maps defined on the whole region of interest of the reference image, and not only on small independent subsets. Such maps are, for instance, based on Finite Element shape functions [31]. Such algorithms have not been considered here.

2.4.2 Gray levels interpolation

Correlation computations often require the estimation of the image gray levels for non integer pixel locations. Interpolation methods used in this paper are: polynomial interpolation (bilinear or bi-cubic), B-spline interpolation (bi-cubic or bi-quintic). Other interpolations based for instance on Fourier or wavelet transforms could be used but have not been investigated in the present work.

2.4.3 Optimization algorithms

In the present work, three optimization strategies are used:

- full optimization: a simultaneous global optimization of all parameters a_i describing the shape function is performed using various nonlinear iterative optimization algorithms, such as first gradient descent, Newton-Raphson, or Levenberg-Marquard.
- partial optimization: the optimization is performed on a restricted set of parameters (typically translation components a_1 and a_2), with fixed (but non-necessarily zero) values of the higher order coefficients. Once this partial optimization is performed for a set of subsets, higher order coefficients relative to a given subset are reevaluated with explicit expressions from the relative displacements of the centers of neighboring subsets, allowing a new estimation of the lower order coefficients. This procedure is iteratively repeated until global convergence of the lower order coefficients.
- Bi-parabolic interpolation of correlation coefficient: when only translation components are to be identified (the other components being set to zero or to a fixed value as for the algorithm described above), a faster alternative to determine their value can be used. It is based on the computation of the correlation coefficient for integer values of the translation components and its interpolation with a bi-parabolic function in the neighborhood of its maximum and its eight nearest neighbors, which can be analytically optimized.

3 Results

3.1 Tested DIC parameter combinations

In order to test the widest range of above described parameter combinations, and since no DIC package implements all of them, the proposed methodology was applied to various academic or commercial softwares used in the French photomechanics community. An additional advantage of this approach is that it allows one to check that the results are linked to the underlying DIC formulation and not the specific software implementation, as very similar results are obtained using two or more independent implementations of a same formulation.

Six DIC softwares were used to obtain the results presented in the following, including two commercial codes, Aramis 2D [46] and Vic-2D [47], and four academic ones : 7D (Université de Savoie), [16], Correla (Université de Poitiers) [48], CorrelManuV (École Polytechnique) [32, 49] and KelKins (Université de Montpellier) [19].

As the purpose of this paper is not to compare the relative performances of these codes, the results will be presented only with a reference to the main parameter combination used for the computation, but no reference to the software.

The following notation[2] will be used to specify the main parameter combinations : $\Phi\phi\mathsf{I}i\mathsf{O}o\mathsf{D}d$, where $\phi \in \{0, 1, 2\}$ refers to the order of the shape function Φ, $i \in \{l, c, q\}$ refers to the gray level interpolation, $o \in \{f, p, b\}$ refers to the optimization procedure (resp. full, partial or bi-parabolic), and d is the width in pixels of the square subset $\mathcal{D}$. Table 1 summarizes the various parameter combinations used in this work with each package.

[Table 1 about here.]

Results, expressed in terms of standard deviation σ, bias $\overline{\Delta u}$ and RMS errors will be analyzed as functions of the set $(p, \alpha, r, \phi, d, i, o, ...)$, keeping in mind that p and α describe the imposed transformation and r characterizes the speckle size. Note that in principle, DIC errors depend also on the signal-to-noise ratio of the images, but this parameter is held constant in our simulations: all images have same bit depth (8 bits) and same gray level histograms, and no additional noise is added.

[2] For instance, $\Phi 1\mathsf{I}l\mathsf{O}f\mathsf{D}16$ corresponds to a DIC formulation with a first order shape function ($\phi = 1$), a bi-linear gray level interpolation ($i = l$), a full optimization ($o = f$) and a 16 pixels subset size ($d = 16$).

For the global analysis, it is observed that the global RMS error is equal to the global standard deviation σ_G since the bias $\overline{\Delta u_G}$ is always very small with respect to σ_G. The reason is that the displacement is periodic with a null average. Since the image size is a multiple of the period, systematic errors are averaged out.

Thus in the next section the global error analysis is restricted to the characterization of the function:

$$RMS_G = \text{function}(p, \alpha, r, \phi, d, i, o, ...) \tag{13}$$

The main features of the results are better explained if they are presented according to the different shape functions Φ used by the DIC packages: translation, affine and quadratic shape function, as illustrated below.

3.2 Global analysis

3.2.1 Translation (zero order shape function)

Fig. 3 illustrates the dependence of RMS_G with respect to the period p of the displacement field for three packages implementing a rigid transformation with various gray level interpolation schemes (see Table 1). All results are relative to the standard pattern (speckle size $r = 2.2$ pixels). Fig. 3(a), relative to a subset size of 31 or 32 pixels, clearly shows the consistency of the results obtained with these packages and a strong dependence of the error with α, which measures the amplitude of the first displacement gradient. Normalization of RMS_G with $u_{,X}^{Max} = 2\pi\alpha$ leads to a single master curve for all packages, independent of α, as shown in Fig. 3(b). Similar observations are made with all tested subset sizes, with an exception for small subset sizes and small strain amplitudes α, as illustrated in Fig. 3(c), where a few curves diverge from the master curve. Fig. 3(d) provides a schematic representation of all the results obtained with various p, α, d and r.

[Figure 3 about here.]

Four main regimes are observed:

- For periods smaller than the subset size d (area I on Fig. 3(d)), it is found that RMS_G is equal to the global RMS of the displacement itself, equal to $\alpha p/\sqrt{2}$. This confirms that DIC algorithms are, as expected, unable to evaluate any displacement fields with spatial fluctuations at a scale smaller than d. The latter can thus be considered as the ultimate spatial resolution of such DIC algorithms.

- In the second and third regime, the error is essentially controlled by α, i.e. the intensity of the first displacement gradient. The existence of a master curve establishes the linear dependence of RMS_G with α. The asymptotic regime of $RMS_G/(2\pi\alpha)$ is obtained for large periods, typically $p \geq 15d$ (area III). In our simulations, it is attained for subset sizes up to $d = 16$ and almost attained for $d = 32$. The independence with p establishes that the algorithm reacts as if the strain was homogeneous in the subset. It is observed that the asymptotic value k_r does not depend on d but depends on the speckle size r as discussed below. In the transition regime (area II, periods between d and about $15d$), RMS_G decreases with the period, but still remains proportional to α.
- In the last regime, observed for small subset sizes ($d \leq 16$ pixels) and small strains ($\alpha = 0.001$), the RMS_G error is larger than $(2\pi\alpha)k_r$ and almost independent of α. It slightly depends on p and reaches an asymptote, denoted σ^t, for large p depending on the subset size and the gray level interpolation scheme in use. For instance, for $d = 10$ pixels, one gets $\sigma^t \approx 0.01$ pixel for bilinear interpolation and $\sigma^t \approx 0.004$ pixel for bi-quintic interpolation. Since this regime is only marginally observed, the dependence of σ^t with d or r could not be investigated in detail.

Since the dominant regime corresponds to area III in Fig. 3(d), additional investigations have been carried out for different speckle pattern sizes: $r_s/2$, r_s and $2r_s$. It is observed that k_r strongly depends on the speckle size r, namely, $k_r \approx 0.35$ pixel for the fine speckle pattern ($r_s/2$), $k_r \approx 0.6$ pixel for the standard speckle pattern (r_s) and $k_r \approx 0.8$ to 1 pixel for the coarse pattern ($2r_s$). In a first approximation, a linear dependency can be adopted: $k_r \approx 0.2r$.

In conclusion, for a zero order shape function (translation), moderately heterogeneous fields and sufficiently large subset, the error is controlled by

$$\Phi = \text{rigid}, \qquad RMS_G = \mathsf{Sup}\left\{k_r(r)\, u_{,X}^{Max}, \sigma^t(d,r,i)\right\}. \tag{14}$$

with $k_r \approx 0.2r$. It is a lower bound in the case of more heterogeneous situations. In most situations, the error is governed by the first term of the supremum, the second being relevant for very small strains.

3.2.2 Affine shape function

Guided by previous results where the error was essentially governed by the first order discrepancy between shape function and actual displacement, results will be presented here using a normalization factor proportional to the maximum of the second gradient, i.e. $u_{,XX}^{Max} = 4\pi^2\alpha/p$. In addition, as it will be demonstrated, in some regimes the error scales with the square of the subset size, so that an appropriate normalization factor is $4d^2\pi^2\alpha/p$. Fig. 4 shows the so-normalized global RMS_G error as a function of period p. Results were obtained with five DIC packages implementing an affine shape function (see Table 1), for the four strain amplitudes α and the standard pattern $r = 2.2$ pixels.

[Figure 4 about here.]

In this representation, a master curve can also be observed for almost all DIC packages, but only for sufficiently large strain and subset. Various curves are observed for a subset size of 10 pixels and for a small strain level ($\alpha = 0.001$), except for large subsets. All these results are gathered in a schematic view (Fig. 4(d)) where, again, four main regimes are observed:

- For small periods $p \leq d$ (area I), it is again found that RMS_G is equal to the global RMS of the displacement itself, confirming that DIC is not able to evaluate any displacement in this situation.

- For periods larger than about $5d$ (area III), an asymptotic value k_a is reached, almost independent of α and d, approximatively equal to 0.03. Small fluctuations (values ranging from 0.026 to 0.033) around this average are observed from one package to another, as a probable consequence of various numerical implementations: optimization algorithm, convergence tolerance, gray level interpolation, etc. To that respect, it is noted that in commercial packages some parameters (such as convergence criteria) are not accessible to the user. As similar trends are observed with academic codes, in which every parameter can be controlled by their author[3], and commercial codes, it is believed that the presented results are representative of the underlying DIC formulation. Small discrepancies between results may be attributed to implementation details but are of second order with respect to the general trends. The error is thus essentially controlled by the second displacement gradient and scales with d^2. The algorithm

---

[3] The authors of the academic codes have participated to this research work and they have run themselves the tests that have lead to the present results.

performs as if the reference image was transformed with a uniform second gradient displacement field. Additional investigations have shown that the asymptotic value k_a is independent of the speckle size in the range $r \in [r_s/2\ ; 2r_s]$. As $RMS_G/(d^2\ u^{Max}_{,XX})$ is an increasing function of p, the asymptotic value k_a provides always an upper bound for the error. The error is thus $RMS_G \leq k_a\ d^2\ u^{Max}_{,XX}$ with $k_a \approx 0.03$.

- The transition regime (area II) observed for periods lying between d and about $5d$ is shorter than for the zero order shape function considered previously. The asymptote is obtained in all cases. One may consider again that the ultimate spatial resolution of the displacement is d itself (beginning of area II).
- However, for small subsets and small strains, as previously observed for rigid shape functions, the asymptotic regime differs. Under such conditions, it is checked that RMS_G reaches an asymptotic value independent on p and α, similar to the asymptotic value $\sigma^t(d, r, i)$ observed for a rigid shape function. A common interpretation of this regime for every shape function order is detailed in Section 4.

To summarize, for an affine shape function, the error is described by

$$\Phi = \text{affine}, \qquad RMS_G \leq \mathsf{Sup}\left\{k_a\ d^2\ u^{Max}_{,XX}, \sigma^t(d, r, i)\right\} \tag{15}$$

The first term is highest for larger strain gradients. It increases with d. The second term is highest for smaller strain gradients. It is demonstrated in Section 4 that it decreases with d, showing that an optimal value of d which depends on abs$(u_{,XX})$ exists. This suggests that optimal DIC algorithms based on affine shape functions, taking into account both the speckle pattern and the strain field to be analyzed could be developed.

3.2.3 Quadratic shape function

RMS_G error versus period p is plotted without any normalization in Fig. 5(a) and 5(b) for the three DIC packages that allow such a choice of shape function (see Table 1). The results obtained with the three packages are qualitatively similar: for $p < d$, as previously, no measurement is ever possible while an asymptotic regime, with RMS_G independent of p and α, is obtained for large p; the transition between these two regimes is rather short, at least for small subset sizes.

[Figure 5 about here.]

For larger subset sizes and small periods, more marginal, intermediate regime governed by the third order displacement gradient is revealed by the normalization of RMS_G with $d^3\ u_{,XXX}^{Max} = 8\pi^3 \alpha d^3/p^2$ (see Figs. 5(c) and 5(d)). This regime is only significant for the packages that lead to the smallest asymptotic values of RMS_G. It induces an error which can be evaluated as $RMS_G \approx k_q\ d^3\ u_{,XXX}^{Max}$ with $k_q \approx 0.0005$.

In the dominant regime, the asymptotic values are dependent on the subset size, as shown in Figs. 5(a) and 5(b). They are also strongly dependent on gray level interpolation and optimization algorithm, as different values are obtained with different packages. The variations of this asymptotic value are similar to those of $\sigma^t(d, r, i)$, but higher values are reached. These points will be discussed more thoroughly in Section 4.

3.3 Local Gradient Analysis

The above global analysis has revealed the existence of situations where the error RMS_G is governed by the discrepancy between the real transformation and the adopted shape function. This dependency of the error will be further investigated in the present section, by correlating local errors and local displacement gradients. This analysis will, in addition, allow us to reveal possible systematic errors linked to the local value of the gradients. For brevity, only results obtained for a subset size equal to $d = 16$ pixels are shown. The same trends are observed for the other subset sizes. Result were obtained with a package implementing a full optimization algorithm and a bilinear interpolation of the gray levels. They are presented according to the different shape functions, as in Section 3.2.

3.3.1 Translation

Fig. 6 allows to retrieve the main result of the global analysis associated with the rigid shape function by considering the whole set of the columns of the image: the mean value of Δu corresponds to $\overline{\Delta u}_G$ for the global analysis and is very small compared with its fluctuations, associated with σ_G.

[Figure 6 about here.]

The local interpretation consists in analyzing the data of each column separately. The fact that the envelope of Δu has the same variations as the displacement gradient $u_{,X}$ suggests that the local standard deviation σ_L is principally related to the local first displacement gradient. Furthermore, for this test, the local gradients and displacements are imposed simultaneously, so no link can clearly be established between Δu and the local displacement. To highlight the influence of the first and second displacement gradients, all the results given by the different combinations of period and strain magnitudes have been gathered. Only results relative to displacement fields with periods larger than $p = 60$ pixels are considered (i.e. situations corresponding to area III and the right hand part of area II in Fig. 3). The local standard deviation, arithmetic mean and RMS error in first displacement gradient / second displacement gradient graphs are presented in Fig. 7.

[Figure 7 about here.]

Both systematic and random errors are functions of the first and second displacement gradients. In order to show their relative influence, the equations fitting the data represented on Fig. 7 are given in the following as functions of the normalized first and second displacement gradients.

As the change in the standard deviation is not dependent on the sign of the displacement gradient, the absolute value of the gradients has been considered to compute the equation describing the data presented in Fig. 7(a) and Fig. 7(c). One gets:

$$\begin{aligned}
\sigma_L &= [A + B\ \mathrm{abs}(g_1) + C\ \mathrm{abs}(g_2) + D\ \mathrm{abs}(g_1)\mathrm{abs}(g_2)] \times 10^{-3} \quad \text{(pixels)} && (16)\\
\overline{\Delta u}_L &= [A + B\ g_1 + C\ g_2 + D\ g_1\ g_2] \times 10^{-3} \quad \text{(pixels)} && (17)\\
RMS_L &= [A + B\ \mathrm{abs}(g_1) + C\ \mathrm{abs}(g_2) + D\ \mathrm{abs}(g_1)\mathrm{abs}(g_2)] \times 10^{-3} \quad \text{(pixels)} && (18)
\end{aligned}$$

where g_1 and g_2 are the normalized first and second displacement gradients respectively, defined by:

$$\left\{ \begin{array}{l} g_1 = \frac{u_{,X}}{u_{,X}^{Max}(\alpha_{max})} = \frac{u_{,X}}{2\pi\alpha_{max}} = \frac{u_{,X}}{0.04\pi} = 7.96\, u_{,X} \\ \\ g_2 = \frac{u_{,XX}}{u_{,XX}^{Max}(\alpha_{max}, p_{min})} = \frac{u_{,XX}}{4\pi^2\alpha_{max}/p_{min}} = \frac{u_{,XX}}{1.33\times 10^{-3}\pi^2} = 76.18\, u_{,XX} \end{array} \right. \qquad (19)$$

with: $\alpha_{max} = 0.02$ and $p_{min} = 60$ pixels. The A, B, C, D coefficients are given in Table 2.

[Table 2 about here.]

The coefficient of the first gradient in Eq. (16) is the most important, showing that in the case of zero order shape function, the standard deviation is mainly dependent on the local first gradient. Furthermore the cross term shows that the effects of the first and second gradients are coupled.

Eq. (17) shows that the arithmetic mean value is either negative or positive, depending on the value of the gradients. The second order gradient has here the preponderant influence and its contribution to this error is about ten times larger than to the standard deviation (Eq. (16)). Note that a positive (resp. negative) second order gradient, i.e. a convex (resp. concave) dependence of displacement with position, leads to an overestimation (resp. underestimation) of the actual displacement by DIC algorithms, as one could expect.

As the coefficient of the second gradient in Eq. (18) is close to its counterpart in Eq. (17), one shows that a large part of the RMS errors linked with the second gradient is due to $\overline{\Delta u_L}$. This term describes the systematic errors, and may thus be corrected. The influence of the first gradient on errors is found both in terms of σ_L (especially for large gradient, see Fig. 7(a)) and $\overline{\Delta u_L}$, because the zero order shape function cannot accurately describe the local displacement field.

3.3.2 Affine and quadratic shape function

When an affine shape function is considered, a similar analysis leads to the dependencies of the errors with the local gradients given in Eqs. (16)-(18) and Table 2.

They confirm the independence of the errors with respect to the first order gradient and the strong influence of the second order gradient. One can check the consistency between this local analysis and the former global one: on the one hand, $RMS_G \approx k_a\, d^2\, u_{,XX}^{Max}$ (see Section 3.2.2) with $k_a \approx 0.03$ and $d = 16$ leads to $RMS_G \approx K_G\, u_{,XX}^{Max}$ with $K_G \approx 7.68$, on the other hand, $RMS_L \approx 130 \times 10^{-3}$ abs(g_2) (see Table 2) and abs$(g_2) = 76.18\, u_{,XX}$ (see Eq. (19)) leads to $RMS_L \approx K_L\, u_{,XX}$ with $K_L \approx 9.9$.

By integrating the local error over all possible positions in a period, we get:

$$RMS_G^2 = \int_0^{2\pi} RMS_L^2(u)du = K_L^2 \int_0^{2\pi} {u_{,XX}^{Max}}^2 \sin^2(u)du = \frac{K_L^2}{2}\, {u_{,XX}^{Max}}^2 = K_G^2\, {u_{,XX}^{Max}}^2 \qquad (20)$$

$K_G \approx 7.68$ and $K_L \approx 9.9$ are consistent with the relation $K_L = \sqrt{2}\, K_G$ extracted from Eq. (20).

As for the zero order shape function, an important conclusion is that the main part of the error is due to the systematic error (arithmetic means, Eq. (17)), but in this case it is only related to the second displacement gradient.

Finally, thanks to the addition of a second gradient in the transformation, the quadratic shape function allows one to minimize the influence of the second displacement gradient on the error. This can be checked on plots similar to Fig. 7, no represented here for the sake of conciseness, on which arithmetic means and standard deviations exhibit now similar values but without any correlation with first and second gradients. One can in addition notice that the amplitude of the standard deviation tends to be somewhat larger in the case of a quadratic shape function than for the affine shape function, when the second gradient is not too high, which suggests that in such a case a lower order shape function might be preferable. This question will be discussed again in Section 4.

4 Discussion

4.1 Error regimes

The observations reported in section 3 allowed us to establish the existence of various DIC error regimes.

The first error regime, which is a known limiting situation for DIC, is for high frequency fields, for which no measurement can be performed when the period of the signal is smaller than the subset size.

In other situations, it has been shown that the asymptotic error can be described by the following relation (see for instance Eqs. (14) and (15)):

$$RMS_G \leq \mathsf{Sup}\left\{\sigma^m, \sigma^t\right\} \tag{21}$$

Whatever the adopted shape function, it is observed that σ^m is proportionnal to the first order term of the discrepancy between the adopted shape function and the actual displacement field in the subset (area III in Figs. 3(d) and 4(d). This observation, confirmed by the local analysis described in section 3.3, extends the results reported in Ref. [34]. σ^m can be linked to the *mismatch error regime*, even if higher order terms might also have an effect (area II and local analysis in section 3.3.1).

For sufficiently small d and small α the asymptotic error is driven by σ^t. This *ultimate error regime* is discussed hereafter.

4.2 Ultimate error independent of local transformation

The ultimate error regime, where RMS_G becomes independent on p and α, and thus is no longer linked to the shape function mismatch, is always observed when a second order shape function is used, whatever d and α. The dependence of the RMS_G error in this regime with the various DIC parameters is now analyzed. Results are gathered in Fig. 8 where the whole set of available asymptotic values of the global analysis for quadratic, affine or rigid shape function and bilinear, bi-cubic or bi-quintic gray level interpolations, for full or partial DIC optimization, are plotted versus the subset size. Note that this limiting regime is not obtained for all combinations of parameters when large subsets are considered. While the influence of subset size d, interpolation i and optimization procedure o have already been mentioned in section 3.2.3, this global plot establishes also the importance of the shape function, especially for small subsets, so that the general expression for this error is $\sigma^t(\phi, d, i, o, r)$. Its dependence with these parameters is now commented with more details, in connection with their influence in the other error regimes.

[Figure 8 about here.]

4.3 Subset Size

A first observation is the strong decrease of $\sigma^t(\phi, d, i, o, r)$ with the subset size d, whatever the DIC formulation. Such a dependence of DIC errors with d has already been observed in the case of pure translation, for instance in Ref. [31] where real transformations have been analyzed. This suggests that $\sigma^t(\phi, d, i, o, r)$ is governed by the same dependencies as in the case of pure translations, even if in the present analysis the transformations are more general. The observed decrease can be explained by the increasing quantity of information, in the form of local gray level gradients, which is used when the subset size is enlarged, leading to a statistical decrease of the errors.

Focusing on results concerning the use of an affine shape function, it is worth noting that the trends observed in Figs. 4 and 8 seem paradoxical. On the one hand, for large strains, there is an increase of the global RMS error with the subset size. The reason for such a deterioration as the subset size increases is due to the fact that the shape function cannot accurately describe the local displacement field, as it is shown in Eq. (18) where the RMS error is only function of the second gradient. On the other hand, for small strains or small subsets, the opposite trend is observed. The local displacement lies inside the chosen space, and thus only the noise reduction effect is felt, namely, the mean of the standard displacement uncertainties decreases as the subset size increases. As a consequence, it is shown that an optimal value of d which depends on $\mathrm{abs}(u_{,XX})$ exists, suggesting that optimal DIC algorithms based on affine shape functions, adapted to the strain field to be analyzed could be developed.

The variations observed in Fig. 5 for which the convergence to the steady value is faster as the subset size is smaller, yet the final value decreases with the subset size, is explained by the same reasons. All these results show that the subset size and the type of shape functions have a strong impact on the displacement uncertainties.

Let us however note that the tendencies observed herein may have a general feature. There exists a first compromise between displacement uncertainty and spatial resolution (i.e. subset size), when the measured displacement is reasonably well described by the local displacement basis. A second limitation is given by the displacement "discretization" (i.e. the subset shape functions) to capture complex displacements. The larger the subsets, the larger the "discretization" error, as observed in finite element procedures. To determine the optimal subset size, known or assumed displacement fields have to be applied to artificial or actual pictures.

4.4 Speckle Size

In the cases under study, the main influence of the speckle size is observed for the asymptotic value of the RMS error, σ^m, when dealing with zero order shape functions. The smaller the correlation radius r, the smaller k_r, which shows that in this case, a reduced speckle size reduces the shape function mismatch error. However, it might also affect the asymptotic error $\sigma^t(\phi, d, i, o, r)$ so that the global effect is not easy to predict. Though the detailed dependencies of $\sigma^t(\phi, d, i, o, r)$ with r have not been studied here, one may expect opposite trends. When r is smaller, the RMS of the gray level gradients in each subset of a given size, i.e. the essential information used for pattern matching, increases, allowing therefore an improved displacement resolution. However, a large pixel size with respect to the pattern size might induce a poor pixel sampling of the actual gray level distribution leading to interpolation errors in the sub-pixel evaluations of displacements. In addition, with current CCD sensors, there are different sources of noise (e.g. dark current noise, readout noise, photon noise) that may corrupt the pictures with a characteristic size equal to one pixel. When the correlation radius is too small (i.e. of the order of one pixel), the signal might no longer be distinguished from this noise so that the conservation of optical flow would significantly degrade.

This suggests again the existence of an optimal compromise between pattern size, pixel size, interpolation scheme, and, in case of a rigid shape function, local strain field. In case of a higher order shape function, it has been observed that speckle size does not significantly affect the shape function mismatch error, σ^m, so that this compromise would not depend on the actual strain field to be measured.

4.5 Gray Level Interpolation

The influence of the gray value intensity interpolation on systematic errors has been studied in Ref. [30] in the case of B-spline interpolator. In this study, DIC algorithm uses the C_{NCC} criteria with affine shape function and a Levenberg-Marquardt iterative search algorithm [47]. Synthetic images are translated and stretched in the Fourier domain with a uniform 0.5% strain. Based on the well-known sinusoidal-shaped curves of the displacement error function of the sub-pixel prescribed displacement [14] obtained both for translation and uniform strain, the authors conclude that high order interpolation reduces the systematic error with a dramatic reduction in going from bilinear to bi-cubic.

While our simulations show that the gray level interpolation scheme has almost no effect on the shape function mismatch error, σ^m, as all packages lead to the same results, Fig. 8 confirms its strong influence when the asymptotic regime $\sigma^t(\phi, d, i, o, r)$ is reached (small strains, small subsets and/or higher order shape functions). The first observation is, as claimed in Ref. [30], a global reduction of the errors by increasing the degree of the interpolation from bilinear to bi-quintic (see Fig. 8 for instance for a first or a second order shape function), especially for small subset sizes.

However, one observes also that the discrepancy between bilinear and bi-cubic is less stringent than in Ref. [30], and that a bi-cubic interpolation might lead to similar or even slightly worse results than a bilinear one for subset sizes d larger than about 20 pixels. Though one cannot exclude that such tendencies might be linked to implementation details, the fact that such a behavior is observed in two independent situations, namely for package 3 with a quadratic shape function, and for package 1 and 2 implementing an affine shape function combined with, respectively, a linear and a bi-cubic interpolation, suggests that this might be an intrinsic feature. A possible reason for it is that in our simulations the limit $\sigma^t(\phi, d, i, o, r)$ is reached for non zero strains, so that the fractional part of the displacement in pixels is not uniform in the subset. Systematic errors correlated with this fractional part might then be smoothed out, especially for large subsets, reducing thus the artifacts induced by a bilinear interpolation (for a subset size of 20 pixels and the smallest strain of 0.63%, the relative motion of pixels within the subset is 0.13 pixels).

Bi-quintic B-spline interpolation leads in all situations to the best results, with an improvement with respect to bilinear interpolation by a factor close to 3. A full analysis of the influence of gray level interpolation would however also require the analysis of the effect of noise in the images in combination with speckle size, as suggested in previous section.

4.6 Subset shape function

The strong influence of the shape function in combination with the subset size on the shape function mismatch error has already been discussed. It appears that the shape function has in addition a strong influence on the ultimate error $\sigma^t(\phi, d, i, o, r)$.

On the one hand a quadratic shape function gives worse results than an affine or a zero order shape function, especially for small subsets. An explanation is that such a shape function requires a large number of parameters to be identified and a small subset may not carry enough information to determine them accurately: remember that DIC is fundamentally an ill-posed inverse problem. This suggests that higher order shape functions should only be used when they are indeed required, i.e. when the mismatch between a lower order shape function and the actual field would be too large.

On the other hand, it is also observed that a rigid shape function leads systematically to larger errors than an affine one, which is in apparent contradiction with above argument. The reason for that might be that in the case of a rigid subset, the limit $\sigma^t(\phi, d, i, o, r)$ is only reached for very small strains and small subsets, i.e. when the displacement is almost uniform in the subset. In such a case, the above mentioned systematic errors are not smoothed out and lead to higher levels of errors.

5 Conclusion

A general procedure to evaluate DIC displacement measurements errors has been proposed. It makes use of synthetic speckle pattern images undergoing spatially fluctuating sinusoidal displacement fields and extends more classical approaches, which address only uniform strain field, to more realistic transformations. RMS errors of the displacements obtained with various DIC formulations could be evaluated as functions of the spatial frequency and the amplitude of the displacement field, for various subset sizes, speckle sizes and other DIC parameters, including shape function and interpolation schemes. Various error regimes could be evidenced and the dependence of the corresponding RMS errors with the DIC and transformation parameters clarified.

When the period p of the displacement fields is smaller than the subset size d, no measurement is possible which confirms that d is the ultimate spatial resolution of DIC measurements. For larger p, two main regimes could be observed. In the first one the error is essentially controlled by the discrepancy between the shape function and the actual displacement field, while in the second one, this discrepancy is sufficiently small so that the error sources are similar to those observed for pure translation, and are independent of the actual transformation.

The first regime is dominant for large subsets, large strains and low order shape functions. For sufficiently large periods, an asymptotic regime of the global RMS error is reached and its value is essentially governed by the first order difference between the real transformation and the used shape function Φ, all other DIC parameters having only a marginal influence. When Φ is a rigid (resp. affine) shape function, the asymptotic error is proportional to the first (resp. second) derivative of the displacement. Moreover, this asymptotic error is independent of d but increases with the speckle size r in the case of a zero order shape function Φ, and scales as d^2 in the case of an affine shape function Φ. The asymptotic regime is obtained faster if d is smaller and if Φ is of higher degree. Note that this regime is only marginally observed when Φ is quadratic; the error is then a proportional to d^3 and the the third derivative of the displacement. A more detailed analysis allows to separate random errors from systematic ones linked with the local values of the displacements gradients at various order, which might be corrected in some improved DIC formulation.

In the second regime, observed for small subsets and small strains and which dominates when Φ is quadratic, the RMS error decreases with subset size d and depends strongly on the interpolation scheme, as already observed for pure translation. It has in addition been shown to depend also on the adopted shape function, the lowest errors being observed for an affine shape function.

The existence of various error regimes in which the dependence of the error with some of the DIC parameters, such as subset size and shape function, are opposite suggest that the optimal choice of these parameters might lead to improved DIC measurements.

Additional investigations, including the analysis of the transition to the asymptotic limit in the first regime, the influence of image noise or the speckle characteristics on $\sigma^t(\phi, d, i, o, r)$, are however required and are the subject of ongoing collaborative work. Studies focusing on the assessment of DIC packages with images subjected to shear strain fields, and assessment of strain measurements by DIC, are also underway.

It is finally worth remembering that the proposed methodology characterizes only a small part of a real DIC measurement chain which involves the correlation algorithm evaluated here, but also the texture to be analyzed, the optical system and its geometrical setup as well as the CCD sensor and its overall properties. These other parts need to be considered as well to fully evaluate the performance of the measurement system that uses surface pictures as input and output values of displacements and displacement errors.

Acknowledgments

The authors and all the participants of this benchmark are grateful to the CNRS for supporting this research.

References

[1] Cloud G. (1998) *Optical Methods of Engineering Analysis*. Cambridge University Press, ISBN 0-521-45087-X.

[2] Rastogi P. (ed.) (1999) *Photomechanics*. Springer Verlag, ISBN 3-540-65990-0.

[3] Molimard J., Lee J., Surrel Y., and Vautrin A. (2002) Full-field optical techniques: applications to strain measurement and mechanical identification. *invited keynote at the 10th European Conference on Composite Materials (ECCM10)*, Bruges, Belgium.

[4] Surrel Y. (2004) Full-field optical methods for mechanical engineering: essential concepts to find one's way. *invited keynote at the 2nd International Conference on Composites Testing and Model Identification*, Bristol, U.K.

[5] Grédiac M. (2004) The use of full-field measurement methods in composite material characterization: interest and limitations. *Composites Part A*, 35:751–761.

[6] Sharpe J. and William N. (eds.) (2007) *Springer Handbook of Experimental Solid Mechanics*. Springer, ISBN 0-387-30877-6.

[7] Patterson E., Hack E., Brailly P., Burguete R., Saleem Q., Siebert T., Tomlinson R., and Whelan M. (2007) Calibration and evaluation of optical systems for full-field strain measurement. *Opt. Las. Eng.*, 45(5):550–564.

[8] Patterson E., Brailly P., Burguete R., Hack E., Siebert T., and Whelan M. (2007) A challenge for high-performance full-field strain measurement systems. *Strain*, 43(3):167–180.

[9] Peters W. and Ranson W. (1982) Digital imaging techniques in experimental stress analysis. *Opt. Eng.*, 21(3):427–431.

[10] Sutton M., Wolters W., Peters W., and McNiell S. (1983) Determination of displacements using an improved digital correlation method. *Image and Vision Computing*, 1:133–139.

[11] Bruck H., McNeill S., Sutton M., and Peters W. (1989) Digital image correlation using Newton-Raphson method of partial differential correction. *Exp. Mech.*, 29:261–267.

[12] Sjödahl M. (1994) Electronic speckle photography – increased accuracy by nonintegral pixel shifting. *J. Appl. Opt.*, 33:6667–6673.

[13] Sjödahl M. (1997) Accuracy in electronic speckle photography. *J. Appl. Opt.*, 36:2875–2885.

[14] Choi S. and Shah S. (1997) Measurement of deformations on concrete subjected to compression using image correlation. *Experimental Mechanics*, 37(3):307–313.

[15] Vendroux G. and Knauss W. (1998) Submicron deformation field: Part 2. Improved digital image correlation. *Exp. Mech.*, 38:85–92.

[16] Vacher P., Dumoulin S., Morestin F., and Mguil-Touchal S. (1999) Bidimensional strain measurement using digital images. *J. Mech. Eng. Sci. C*, 213:811–817.

[17] Doumalin P., Bornert M., and Caldemaison D. (1999) Microextensometry by image correlation applied to micromechanical studies using the scanning electron microscopy. *Proceedings of the International Conference on Advanced Technology in Experimental Mechanics, Japan Soc. of Exp. Eng.*, Ube City, Japan, pp. 81–86.

[18] Sutton M., McNeill S., Helm J., and Chao Y. (2000) Advances in Two-Dimensional and Three-Dimensional Computer Vision. Rastogi P. (ed.), *Photomechanics*, Topics in Applied Physics, Springer Verlag, Berlin.

[19] Wattrisse B., Chrysochoos A., Muracciole J.-M., and Némoz-Gaillard M. (2001) Analysis of strain localization during tensile tests by digital image correlation. *Experimental Mechanics*, 41(1):29–39.

[20] Chevalier L., Calloch S., Hild F., and Marco Y. (2001) Digital image correlation used to analyze the multiaxial behavior of rubber-like materials. *Eur. J. Mech. A - Solids*, 20:169–187.

[21] Wang Y. and Cuitiño A. (2002) Full-field measurements of heterogeneous deformation patterns on polymeric foams using digital image correlation. *International Journal of Solids and Structures*, 39:3777–3796.

[22] Abanto-Bueno J. and Lambros J. (2002) Investigation of crack growth in functionally graded materials using digital image correlation. *Engineering Fracture Mechanics*, 69:1695–1711.

[23] Laraba-Abbes F., Ienny P., and Piques R. (2003) A new 'tailor-made' methodology for the mechanical behaviour analysis of rubber-like materials: I. Kinematics measurements using a digital speckle extensometry. *Polymer*, 44:807–820.

[24] Zhang J., Xiong C., Li H., Li M., Wang J., and Fang J. (2004) Damage and fracture evaluation of granular composite materials by digital image correlation method. *Acta Mechanica Sinica*, 20(4):408–417.

[25] Parsons E., Boyce M., and Parks D. (2004) An experimental investigation of the large-strain tensile behavior of neat and rubber-toughened polycarbonate. *Polymer*, 45:2665–2684.

[26] Bergonnier S., Hild F., and Roux S. (2005) Digital image correlation used for mechanical tests on crimped glass wool samples. *J. Strain Analysis*, 40(2):185–198.

[27] Yoneyama S., Morimoto Y., and Takashi M. (2006) Automatic evaluation of mixed-mode stress intensity factors utilizing digital image correlation. *Strain*, 42:21–29.

[28] Réthoré J., Gravouil A., Morestin F., and Combescure A. (2005) Estimation of mixed-mode stress intensity factors using digital image correlation and an interaction integral. *Int. J. Fract.*, 132:65–79.

[29] MCIMS (2003), Mesures de Champs et Identification en Mécanique des Solides / Full field measurement and identification in solid mechanics, `http://www.ifma.fr/lami/gdr2519/`.

[30] Schreier H., Braasch J., and Sutton M. (2000) Systematic errors in digital image correlation caused by intensity interpolation. *Opt. Eng.*, 39(11):2915–2921.

[31] Hild F. and Roux S. (2006) Digital image correlation: from displacement measurement to identification of elastic properties - a review. *Strain*, 42(2):69–80.

[32] Doumalin P. (2000) *Microextensométrie locale par corrélation d'images numériques ; application aux études micromécaniques par microscopie électronique à balayage*. Ph.D. thesis, École Polytechnique, Palaiseau (France).

[33] Garcia D. (2001) *Mesure de formes et de champs de déplacements tridimentionnels par stéréo-corrélation d'images*. Ph.D. thesis, Institut National Polytechnique de Toulouse (France).

[34] Schreier H. and Sutton M. (2002) Systematic errors in digital image correlation due to undermatched subset shape functions. *Experimental Mechanics*, 43(3):303–311.

[35] Knauss W. G., Chasiotis I., and Huang Y. (2003) Mechanical measurements at the micron and nanometer scales. *Mechanics of Materials*, 35(3-6):217–231.

[36] Lecompte D., Smits A., Bossuyt S., Sol H., Vantomme J., Van Hemelrijck D., and Habraken A. (2006) Quality assessment of speckle patterns for digital image correlation. *Optics and Lasers in Engineering*, 44:1132–1145.

[37] Réthoré J., Hild F., and Roux S. (2008) Extended digital image correlation with crack shape optimization. *Int. J. Num. Meth. Eng.*, 73(2):248–272.

[38] Orteu J.-J., Garcia D., Robert L., and Bugarin F. (2006) A speckle-texture image generator. *Proceedings of the Speckle'06 International Conference*, Nîmes, France.

[39] Perlin K. (1985) An Image Synthesizer. *Proceedings of the SIGGRAPH'85 Conference*, San Francisco, California, USA, pp. 287–296.

[40] Rubin D. (2004) A simple autocorrelation algorithm for determining grain size from digital images of sediment. *Journal of Sedimentary Research*, 74(1):160–165.

[41] Besnard G., Hild F., and Roux S. (2006) "finite-element" displacement fields analysis from digital images: Application to Portevin-Le Châtelier bands. *Exp. Mech.*, 46:789–803.

[42] Horn B. and Schunk B. (1981) Determining optical flow. *Artificial intelligence*, 17:185–202.

[43] Lu H. and Ganesan B. (2002) Displacement gradient in digital image correlation. *Proceedings of the 2002 International Conference on Computational Engineering and Science*.

[44] Lu H. and Cary P. (2000) Deformation measurements by digital image correlation: Implementation of a second-order displacement gradient. *Experimental Mechanics*, 40(4):393–400.

[45] Chambon S. and Crouzil A. (2003) Dense matching using correlation: new measures that are robust near occlusions. *Proceedings of British Machine Vision Conference (BMVC'2003)*, East Anglia, Norwich, UK, pp. 143–152.

[46] Aramis 2D software (2008), GOM Optical Measuring Techniques, `http://www.gom.com/EN/index.html`.

[47] Vic-2D software (2008), Correlated Solutions Inc., `http://www.correlatedsolutions.com/`.

[48] Germaneau A., Doumalin P., and Dupré J. (2007) Full 3D Measurement of Strain Field by Scattered Light for Analysis of Structures. *Exp. Mech.*, 47(4):523–532.

[49] N. Lenoir N., Bornert M., Desrues J., Bésuelle P., and Viggiani G. (2007) Volumetric digital image correlation applied to x-ray microtomography images form triaxial compression tests on argillaceaous rocks. *Strain*, 43:193—205.

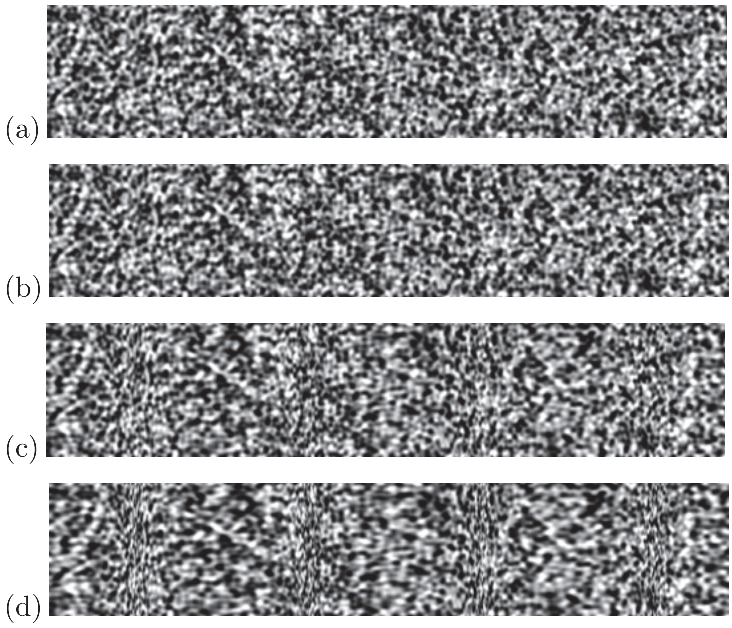

Figure 1: Example of simulated synthetic images: reference (a) and deformed images ($p = 130$ pixels, (b) $\alpha = 0.02$ - $u_{,X}^{Max} = 12.6\%$, (c) $\alpha = 0.05$ - $u_{,X}^{Max} = 31.4\%$ and (d) $\alpha = 0.1$ - $u_{,X}^{Max} = 62.8\%$).

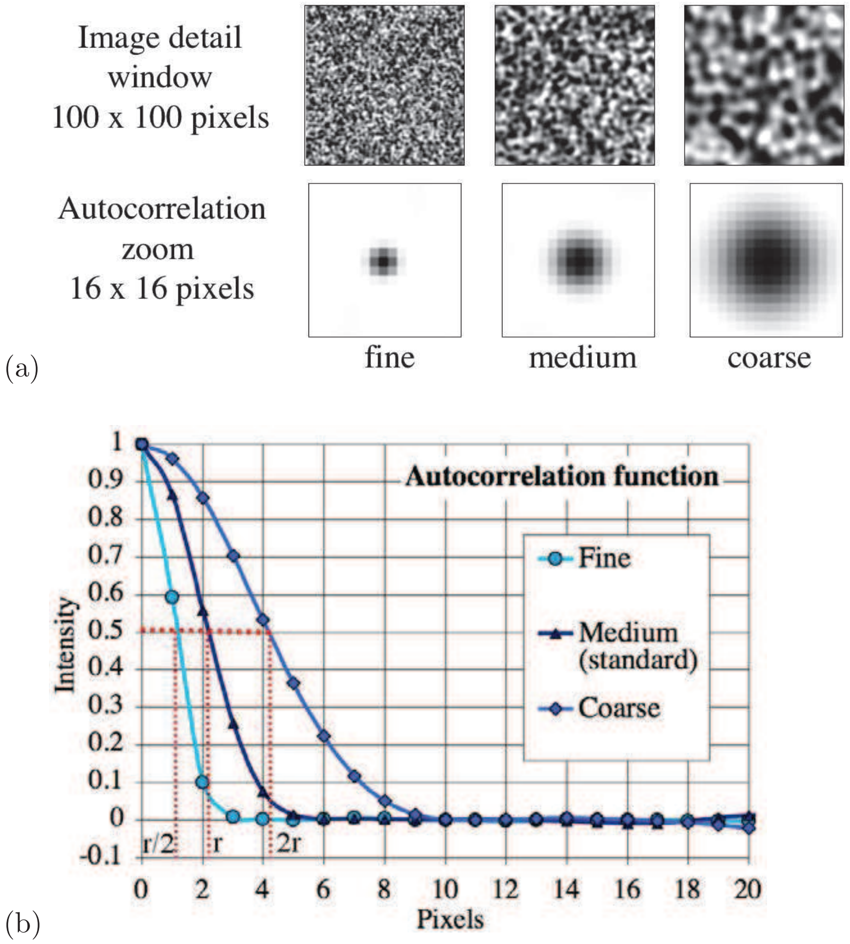

Figure 2: Illustration of synthetic speckle patterns. (a) fine, medium and coarse patterns and (b) associated centered and normalized autocorrelation function radius at half height.

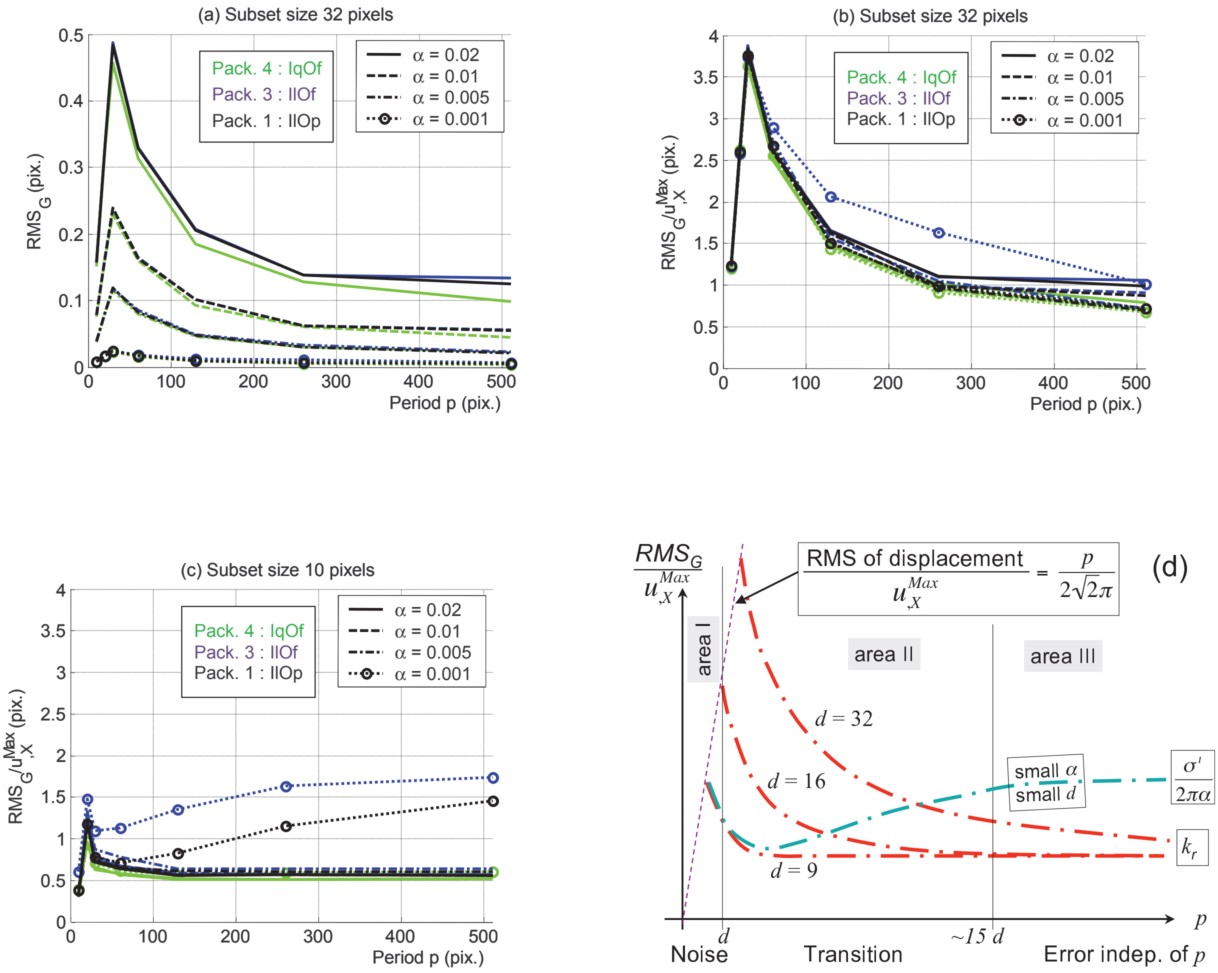

Figure 3: Evolutions of RMS_G with parameters p, α and d, obtained with three packages implementing a zero order shape function and various gray level interpolations. Speckle size $r = 2.2$ pixels. (a) RMS_G as a function of p, subset size $d = 32$ pixels, (b) $RMS_G/(2\pi\alpha)$ as a function of p, subset size $d = 32$ pixels, (c) $RMS_G/(2\pi\alpha)$ as a function of p, subset size $d = 10$ pixels, (d) Schematic representation of all observations.

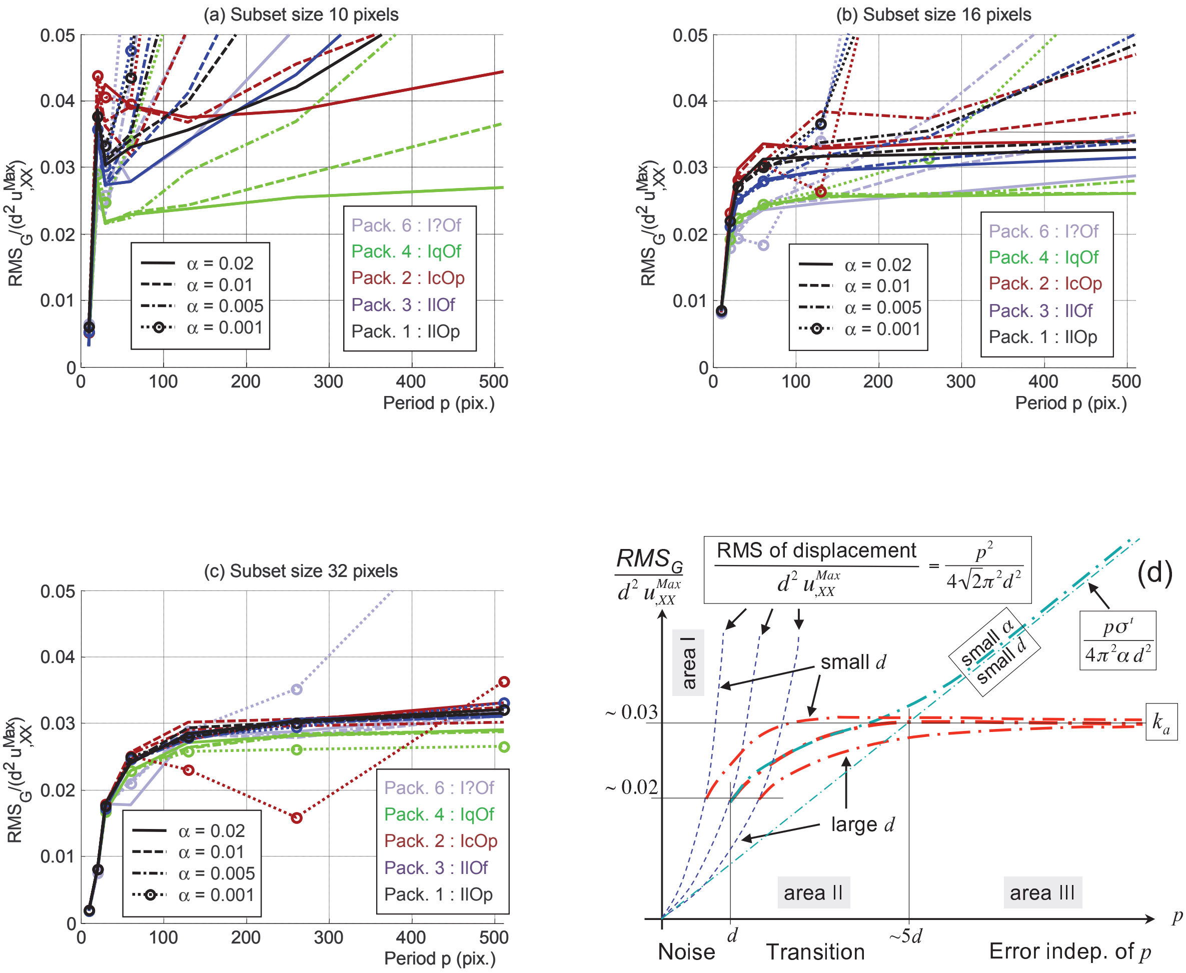

Figure 4: RMS_G normalized by $4d^2\pi^2\alpha/p$ as a function of period p, for various strain amplitudes α, for an affine shape function and for five DIC packages (20 curves). Subset size d is equal to 10, 16 and 32 pixels in plots (a), (b) and (c), respectively. (d) is a schematic representation of all observations.

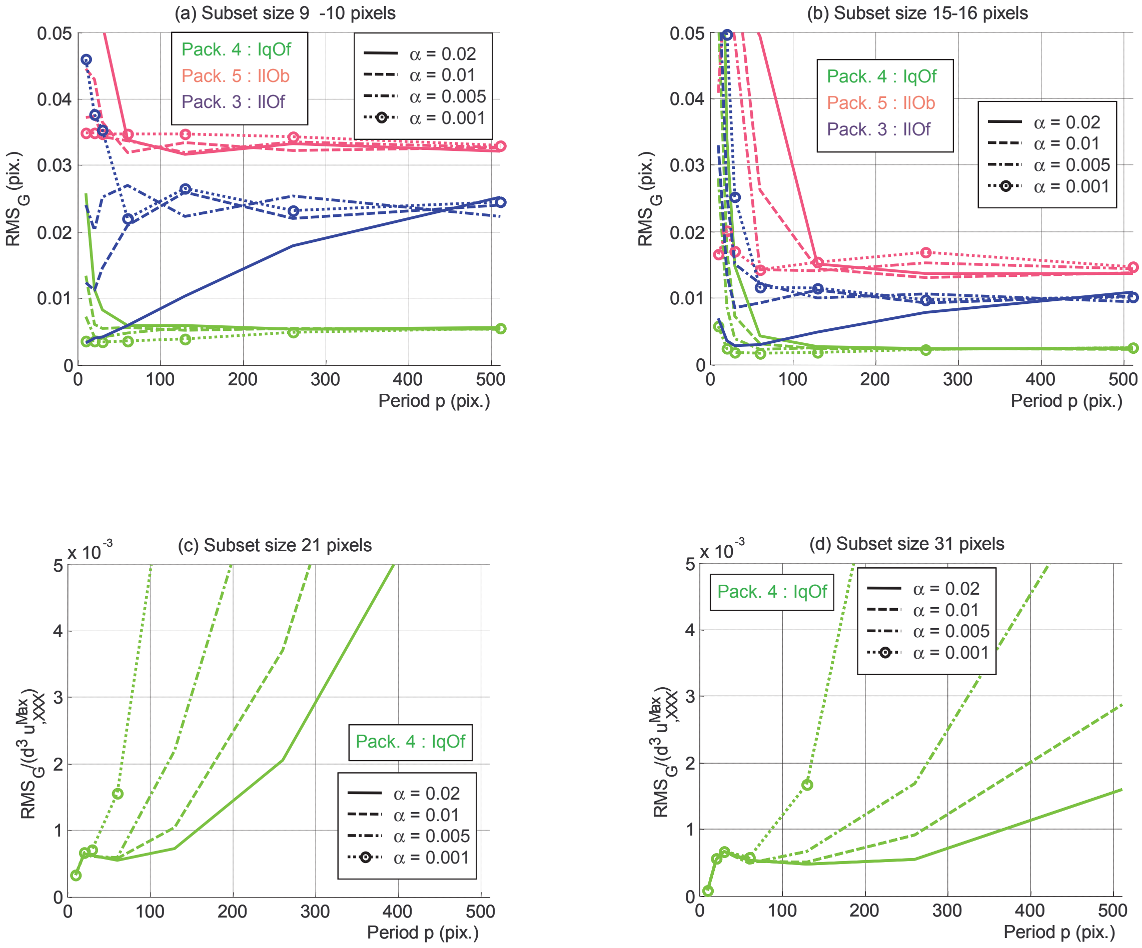

Figure 5: RMS_G as a function of period p for various strain amplitude α, for a quadratic shape function and for three DIC packages. Subset size d is equal to 9 or 10 (a), 15 or 16 (b), 21 (c) and 31 pixels (d) respectively. The error is not normalized in (a) and (b), while it is divided by $8\pi^3\alpha d^3/p^2$ in (c) and (d); only one DIC package is represented in (c) and (d).

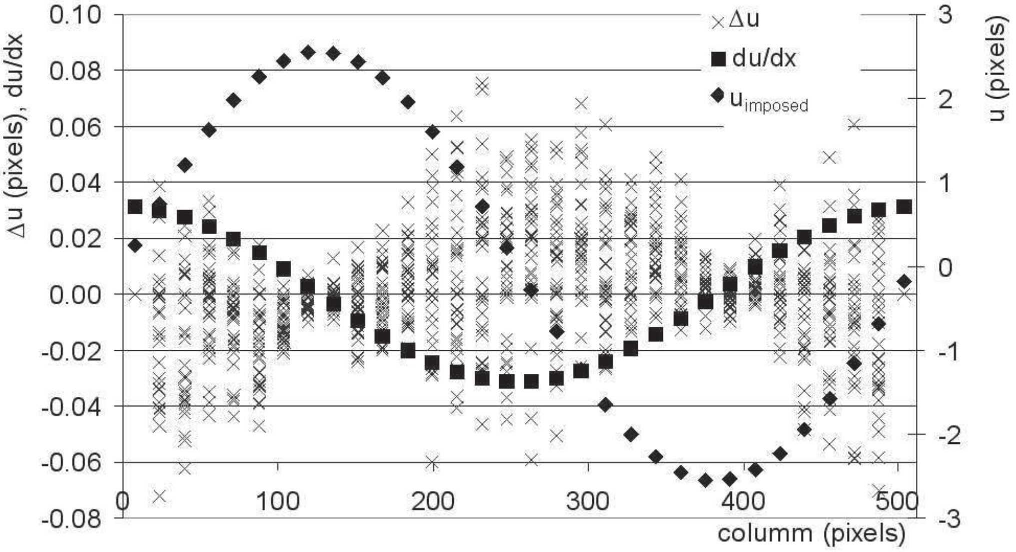

Figure 6: Imposed displacement, displacement gradient and local error $\Delta u(i,j)$ as a function of the column of the image ($\alpha = 0.005$, $p = 510$ pixels, $d = 16$ pixels, zero order shape function Φ, $u^{Max} = \alpha p = 2.55$ pixels, and $\left(\dfrac{du}{dx}\right)^{Max} = u^{Max}_{,X} = 2\pi\alpha = 3.1\%$).

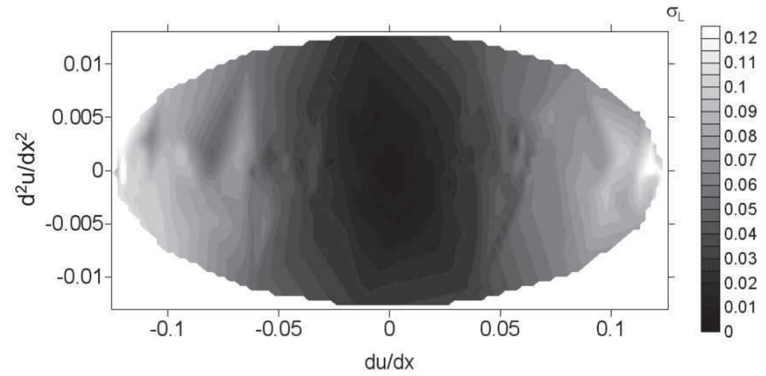

(a) Local standard deviation σ_L

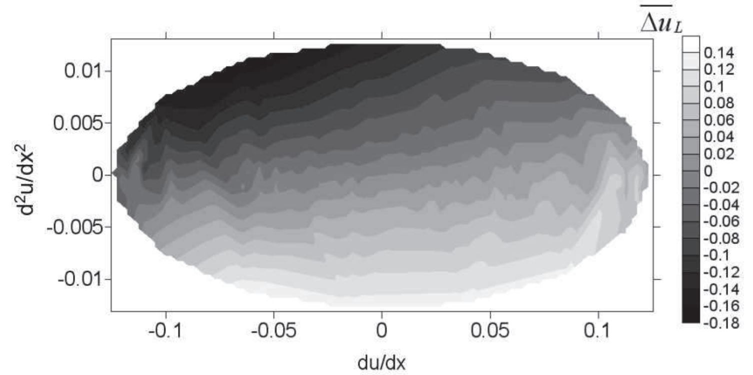

(b) Local Arithmetic mean $\overline{\Delta u}_L$

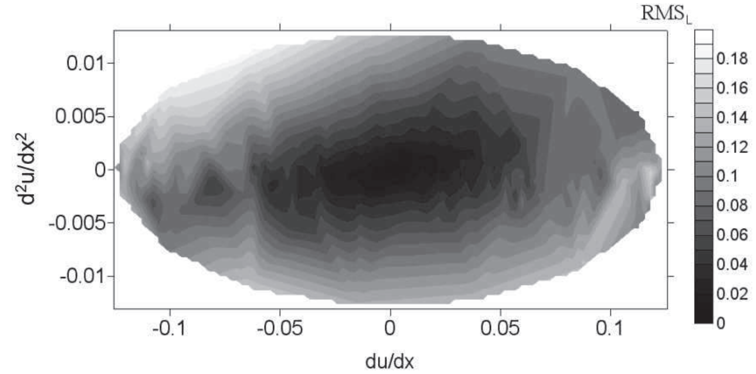

(c) Local RMS error RMS_L

Figure 7: Influence of the first and second displacement gradients ($d = 16$ pixels, zero order shape function Φ).

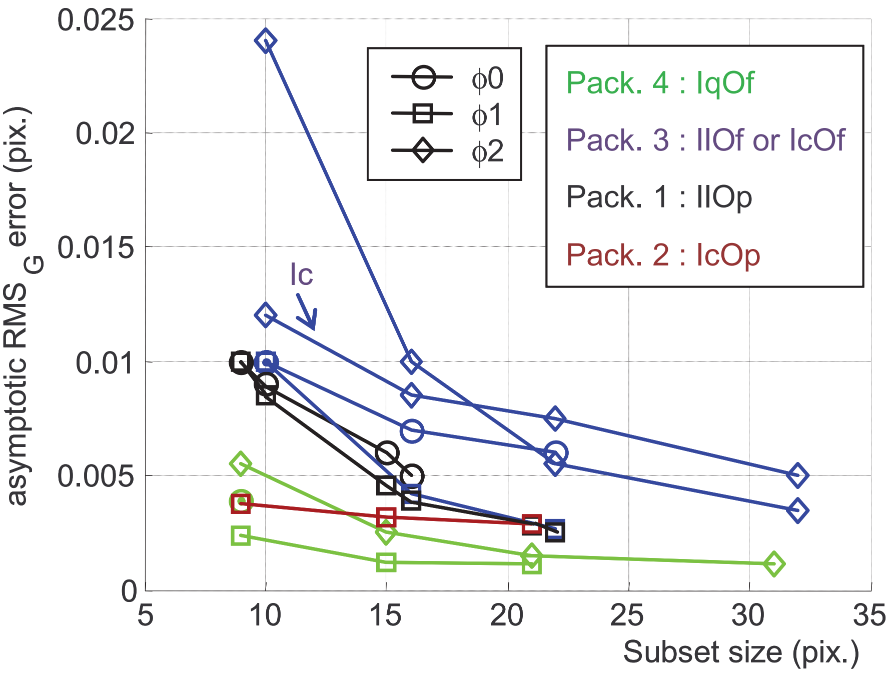

Figure 8: Comparison of the asymptotic RMS error $\sigma^t(\phi, d, i, o, r)$ for quadratic, affine or rigid shape function and bilinear, bi-cubic or bi-quintic gray level interpolations as a function of the subset size. Speckle size is $r = 2.2$ pixels.

Package #	ϕ	i	o	d
1	$0, 1$	l	p	any
2	1	c	p	odd
3	$0, 1, 2$	l, c	f	even
4	$0, 1, 2$	q	f	odd
5	2	l	b	odd
6	1	?	f	odd

Table 1: DIC packages and associated parameter combinations used in the present study.

		A	B	C	D
Rigid shape function	σ_L	0.8	114	15.5	-41.3
	$\overline{\Delta u}_L$	-0.44	54	-146	-45.9
	RMS_L	-1.48	123	137	-141
Affine shape function	σ_L	2.5	1.63	18	-4.1
	$\overline{\Delta u}_L$	-0.16	-0.0804	-135	-2.51
	RMS_L	1.48	0.302	130	-1.48

Table 2: Coefficients of the surface equations given in Eqs. (16)-(18) and derived from rigid shape function results (Figure 7) and affine shape function results.